

Pore structure and tracer migration behavior of typical American and Chinese shales

Qin-Hong Hu^{1,2} · Xian-Guo Liu¹ · Zhi-Ye Gao³ · Shu-Gen Liu⁴ · Wen Zhou⁴ · Wen-Xuan Hu⁵

Received: 11 May 2015 / Published online: 16 September 2015
© The Author(s) 2015. This article is published with open access at Springerlink.com

Abstract With estimated shale gas resources greater than those of US and Canada combined, China has been embarking on an ambitious shale development program. However, nearly 30 years of American experience in shale hydrocarbon exploration and production indicates a low total recovery of shale gas at 12 %–30 % and tight oil at 5 %–10 %. One of the main barriers to sustainable development of shale resources, namely the pore structure (geometry and connectivity) of the nanopores for storing and transporting hydrocarbons, is rarely investigated. In this study, we collected samples from a variety of leading hydrocarbon-producing shale formations in US and China. These formations have different ages and geologic characteristics (e.g., porosity, permeability, mineralogy, total organic content, and thermal maturation). We studied their pore structure characteristics, imbibition and saturated diffusion, edge-accessible porosity, and wettability with four complementary tests: mercury intrusion porosimetry, fluid and tracer imbibition into initially dry shale, tracer

diffusion into fluid-saturated shale, and high-pressure Wood's metal intrusion followed with imaging and elemental mapping. The imbibition and diffusion tests use tracer-bearing wettability fluids (API brine or n-decane) to examine the association of tracers with mineral or organic matter phases, using a sensitive and micro-scale elemental laser ablation ICP-MS mapping technique. For two molecular tracers in n-decane fluid with the estimated sizes of 1.39 nm × 0.29 nm × 0.18 nm for 1-iododecane and 1.27 nm × 0.92 nm × 0.78 nm for trichlorooxobis (triphenylphosphine) rhenium, much less penetration was observed for larger molecules of organic rhenium in shales with median pore-throat sizes of several nanometers. This indicates the probable entanglement of sub-nano-sized molecules in shales with nano-sized pore-throats. Overall findings from the above innovative approaches indicate the limited accessibility (several millimeters from sample edge) and connectivity of tortuous nanopore spaces in shales with spatial wettability, which could lead to the low overall hydrocarbon recovery because of the limited fracture–matrix connection and migration of hydrocarbon molecules from the shale matrix to the stimulated fracture network.

✉ Qin-Hong Hu
water19049@gmail.com

¹ China University of Geosciences (Wuhan), Wuhan 430074, China

² The University of Texas at Arlington, Arlington, TX 76019, USA

³ State Key Laboratory of Petroleum Resources and Prospecting, China University of Petroleum, Beijing 102249, China

⁴ State Key Laboratory of Oil and Gas Reservoir Geology and Exploitation, Chengdu University of Technology, Chengdu 610059, China

⁵ Nanjing University, Nanjing 210093, China

Edited by Xiu-Qin Zhu

Keywords Shale · Nanopore · Connectivity · Diffusion · Imbibition

1 Introduction

Since 2000, the technological development of horizontal drilling and hydraulic fracturing in US has led to a dramatic increase in hydrocarbon (gas and oil) production from shale formations, changing the fossil energy outlook in the US and worldwide (DOE 2009; Jarvie 2012; EIA 2014).

The production of shale hydrocarbon has recently increased significantly, and it is predicted that the production of shale gas will account for 50 % of total dry gas production in the USA by 2040, an increase from 34 % in 2011 (EIA 2014). Likewise, US tight oil production is 1.8 million barrels per day (accounting for 28 % of total US production) in 2012 and 2.8 million barrels (35 %) in 2013, and projected to be 4.8 million barrels in 2019 to provide more than a quarter of the 18.8 million barrels of oil that the US currently consumes daily.

Despite the increased gas and oil production from shale formations, analyses of data from 65,000 shale wells in 30 shale gas and 21 tight oil fields in the US led Hughes (2013a, b) to argue that the shale revolution will be hard to sustain. The data indicate that the production from a given well would decline rapidly within a few years. For example, wells in the top five US shale gas (Marcellus, Haynesville, Barnett, Fayetteville, and Eagle Ford) plays typically produce 80 %–95 % less gas after 3 years, and the productivity of new wells in two leading tight oil plays (Bakken and Eagle Ford) drops by about 60 % within the first year. The total gas recovery from the Barnett, the most developed shale play, is reported to be only 8 %–15 % of gas-in-place in 2002 (Curtis 2002), and 12 %–30 % in 2012 (King 2012). The recovery rate for tight oil is even lower at 5 %–10 % (Hoffman 2012), for example, the oil recovery rate in the middle member Bakken formation ranges from 2 % to 5 % to as high as 20 % (Jarvie 2012).

With estimated shale gas resources greater than that of US and Canada combined, China has been embarking on an ambitious shale development program. China has several types of shale (by area: 26 % marine, 56 % marine-terrestrial transitional, and 18 % terrestrial), whereas nearly all the US producing shales are of marine type (Zou et al. 2013). Sinopec (China) has recently reported that its first marine shale well (Jiao-Ye #1HF, drilled on Feb. 14, 2012 and completed on Nov. 24, 2012) initially produced $2.0 \times 10^5 \text{ m}^3$ gas/day, and maintained a stable daily production of $6.6 \times 10^4 \text{ m}^3$ over the next 7 months. This production behavior, though of limited duration, is consistent with the 60 % 1st-year decline observed in US shale wells.

Shale geology could be a bottleneck to its sustainable development. While Hughes' articles (2013a, b) mentioned this steep decline and low overall recovery, investigations into their root cause(s) are surprisingly scarce (Hu and Ewing 2013). This work highlights the studies of root causes from pore structure and fluid migration in the tight matrix of several leading US and China shales. China has so far drilled about 300 shale wells, dwarfed by the 80,000 US wells. A comparative analysis of pore structure and its resultant fluid migration behavior is critically important. Low recovery, coupled with the relatively high cost of

shale hydrocarbon development and the sharp drop in oil price that started in 2014, is the main barrier to sustainable development of US and China shale.

Fluid flow and solute transport in rock are macroscopic consequences of the pore structure, which integrates geometry (e.g., pore size and shape, pore size distribution; Bear 1972) and topology (e.g., pore connectivity; Dullien 1992). Especially when pore connectivity is low, topological factors outweigh the better known geometrical factors (Ewing and Horton 2002; Hu et al. 2012; Hunt et al. 2014). However, the prevalence of low pore connectivity in tight shales, and its impacts on fluid flow and chemical transport, is poorly documented and understood. This work examines the potential of low pore connectivity of typical American and Chinese shales, and its effects on fluid flow and chemical transport.

2 Materials and methods

2.1 Samples

The research objective of this work is to examine the pore structure (especially connectivity) characteristics of several shale samples from active and leading onshore US and China plays for hydrocarbon production (Table 1). These shale samples have different geologic ages, mineralogy, total organic carbon (TOC), kerogen types, and maturation levels. For example, the Chinese shales generally have much higher thermal maturation (with R_0 values at about 3 %) than American ones (Table 1). Various geologic controls on pore connectivity have not been systematically studied in the literature.

Located in the Fort Worth Basin in north-central Texas, the Barnett shale (the birth place of the “shale revolution”) is a Mississippian-age marine shelf deposit, ranging in thickness from about 60 m (200 feet) in the southwest region to 305 m (1000 feet) to the northeast. The formation is a black, organic-rich shale (total organic carbon at 0.4 %–10.6 %, with an average of 4.0 %; Loucks and Ruppel 2007) composed of fine-grained, siliciclastic rocks with low permeability (70–5000 nD [nano-Darcy]) (Grieser et al. 2008; Loucks et al. 2009). The Barnett shale play currently has some 18,000 producing wells (Nicot et al. 2014). The reservoir produces at commercially viable levels only with hydraulic fracturing that establishes long and wide fractures, which connect large surface areas of the formation through a complex fracture network. However, gas production in such tight shale is still technically challenging, partly from the lack of the understanding of nanopore structure characteristics of the shale matrix.

The 120 foot long (37 m) Blakely #1core (API 42-497-33041), taken from southeastern Wise County within the

Table 1 Typical hydrocarbon-producing shales in China and USA tested in this work

Well/ sample ID	Formation	Geologic age (millions years ago)	Depth below ground, m	Location	TOC, wt%	R_o , %
EF outcrop	Eagle Ford (EF)	Late Cretaceous (99.6–65.5)	Surface outcrop	Comstock, Val Verde Co., TX	5.3	0.53
Leppard #1 (LP)			4143.9–4165.8	Bee Co., TX	NA	NA
Blakely #1 (BL)	Barnett (B)	Mississippi (359.2–318.1)	2166.8–2200.4	Wise Co., TX	3.08–6.62	~1.35
TZ-4H	Longmaxi (LMX)	Early Silurian (443.7–428.2)	Surface outcrop	Qilong Village, Xishui, Guizhou	6.23	NA
Jinye Well No. 1	Niutitang (NTT; also known as Qiongzhusi)	Early Cambrian (542.0–513.0)	136.7–220.5	Wazhi Village, Liujiashen, Rong County, Sichuan	0.2–11.5	2.11–3.74
YC01-72D	Doushantuo (DST)	Sinian (800–570)	Surface outcrop	Jiulongwan, Yichang, Hubei	9.68	NA

Average of 31 Barnett core samples from 4 wells including Blakely #1 (Loucks and Ruppel 2007)

NA not available

Fort Worth Basin, includes part of the upper Barnett Shale (2166–2169 m below ground surface (bgs), the Forestburg Limestone (2169–218 mbgs), and the upper part of the lower Barnett Shale (2181–2202 mbgs) (Loucks and Ruppel 2007). We obtained core samples from this Blakely #1 well, courtesy of the core repository of the Texas Bureau of Economic Geology, representing five depths separated by at most 10 m: 2167 m (7109 ft; upper Barnett), 2175 m (7136 ft; Forestburg Limestone), and 2185 m (7169 ft), 2194 m (7199 ft) and 2200 m (7219 ft); all from the upper part of the lower Barnett) (Table 2).

Since around 2008, U.S. natural gas drillers, stung by decade-low gas prices from the over-supply of shale gas, have focused significant efforts on producing oil from the liquids-rich shale plays, such as Eagle Ford. The Eagle Ford shale of southeast Texas, covering 23 counties, is currently one of the most active shale hydrocarbon plays in the U.S. It trends across Texas from the Mexican border up into East Texas, roughly 80 km wide and 644 km long with an average thickness of 76 m, at depths ranging from 1220 to 3660 ft. The amount of technically recoverable oil in the Eagle Ford is estimated by the U.S. DOE to be 3.35 billion barrels of oil. The high percentage of carbonate makes the Eagle Ford shale brittle and “fracable” for the production of oil, condensate, and gas.

Eagle Ford shale samples in this work come from two sources: an outcrop and core samples from several depths. The Comstock West outcrop sample from Val Verde Co. was collected in Highway 90 about 50 km north-west of Del Rio, Texas (Slatt et al. 2012). The outcrop sample has an average TOC value of 5.3 %, and contains Type II kerogen, making it an excellent marine oil and gas source rock. However, at this location, the rocks are thermally immature with T_{max} values of 423–429 °C and average R_o

of 0.53 %. The sample is calcareous with an average $CaCO_3$ content of 64 %. Core samples from the J.A. Leppard #1 well (API 42-025-30389) in Bee County were obtained from the Texas Bureau of Economic Geology.

Samples from three typical shale formations in southwest China are studied in this work (Table 1): they are cores from an exploratory shale well (Jinye Well No. 1), and surface samples from two well-studied outcrops in Xishui Qilong Village for the Longmaxi Formation and Xiadong Jiulongwan for the Doushantuo Formation (Xie et al. 2008).

The Sichuan basin is an oil-bearing and gas-rich basin with an extensive development of the Lower Silurian Longmaxi Formation shale in southwestern China (southeastern Sichuan and western Hubei-eastern Chongqing) (Zou et al. 2013). The Longmaxi Formation contains 0.2 %–6.7 % of total organic carbon. The organic matter is over-mature, with R_o ranging from 2.4 % to 3.6 %, and dominated by Type II kerogen. Porosity measured on core samples of the shale from the Longmaxi Formation in exploratory wells ranges from 0.58 % to 0.67 % (Liu et al. 2011). The microporosity observed in thin sections of the shale is about 2 %, and dominated by intercrystalline and intragranular pores, with the pore size ranging from 100 nm to 50 μ m. There are some differences between the Longmaxi Formation shale and the Barnett shale. The former is buried more deeply, with a higher degree of thermal evolution, lower gas content, denser, and more quartz of terrigenous origin (Liu et al. 2011).

In the Sichuan basin and its surrounding areas, shale gas in Lower Cambrian Niutitang Formation is distributed over all areas except for the eroded region in West Sichuan. Generally thicker than 40 m, its thickness increases from the central Sichuan to the north, the east, and the south. The

Table 2 Basic pore structure characteristics from MICP analyses

Sample ID ^a	Porosity, %	Total pore area, m ² /g	Median pore-throat diameter (volume), nm ^b	Characteristic length, nm ^c	Permeability, nD	Effective Tortuosity ^d	L_e/L^d
EF outcrop	7.85	6.38	22.7	7.2	258	80.5	2.51
EF LP4146 ^e	3.28	7.16	6.5	4.1	2.72	1814	7.71
EF LP4155	1.56	3.14	9.5	3.2	1.60	NA	NA
EF LP4155 ^e	2.58	5.49	8.0	3.2	2.46	2815	8.52
EF LP4157	3.11	5.58	17.4	6.4	2.97	2191	8.26
EF LP4166 ^e	1.75	2.48	23.5	3.2	1.60	3867	8.23
B BL2167	1.98	4.87	5.9	4.8	1.35	2136	6.51
B BL2167	1.54	3.67	6.1	3.5	1.48	2026	5.58
B BL2175 ^e	0.294	0.061	2698	13.7	3.24	1759	2.27
B BL2175	0.223	0.225	30.0	12.2	1.18	1784	1.99
B BL2185 ^e	0.711	1.01	21.9	5.2	0.52	8699	7.86
B BL2185	0.555	1.02	7.0	4.6	1.05	2045	3.37
B BL2194	5.08	13.5	5.9	4.5	4.22	2273	10.7
B BL2194	4.84	13.0	5.9	4.0	3.71	2316	10.6
B BL2200	3.89	9.25	6.5	4.5	2.65	3845	12.2
B BL2200	3.27	7.51	6.7	3.6	2.78	3694	11.0
LMX TZ-4H	3.83	10.3	6.3	3.0	3.91	NA	NA
LMX TZ-4H	5.45	17.5	5.0	3.1	5.38	2214	11.0
NTT JY#1-137	1.49	1.01	65.9	11.0	9.58	NA	NA
NTT JY#1-137	1.18	1.10	20.9	6.5	1.99	1805	4.62
NTT JY#1-189	1.44	2.61	11.5	3.3	1.35	NA	NA
NTT JY#1-189	1.80	3.62	8.7	4.0	1.60	3683	8.13
NTT JY#1-220	3.91	9.07	8.3	3.3	3.66	NA	NA
NTT JY#1-220	4.39	7.86	10.3	5.7	6.64	1068	6.84
NTT JY#1-220	2.33	8.25	4.1	3.8	1.99	4103	9.77
DST YC01-72D	7.81	6.86	41.5	4.0	5.88	1413	10.5

^a Numbers are the sample depths in a well (e.g., BL-2167 denotes sample location at 2167 m of the Blakely #1 well)

^b Pore-throat diameter at which the volume of intruded mercury is 50 % of final value

^c The characteristic (or threshold) length which is the pore-throat diameter corresponding to the threshold pressure P_t (psia); P_t is determined at the inflection point of the cumulative intrusion curve when mercury starts to percolate the whole sample

^d NA not available. Some early measurements do not produce the effective tortuosity results, as the tortuosity calculation uses data points beyond the threshold pressure which is near 3-nm lower limit of the MICP instrument; recent measurements with more pressure measurement points consistently generate the tortuosity values

^e These two sample cubes are detected to contain micron size fractures which lead to larger median pore-throat diameters than their non-fractured duplicate sample

Niutitang shale has a high organic carbon content, more than 2 % in most areas of Sichuan Basin. This formation is mature or over-mature. It is also deeply buried (more than 7 km in the west, the north and the east), and has evolved for a long time with complex preservation conditions which inhibit exploration and development. The most favorable exploration region lies in the south of Sichuan Basin, and the second most favorable areas are in western Hubei and eastern Chongqing (Liu et al. 2011; Sun et al. 2011; Guo 2013). Jinye well No. 1 is the first Sinopec shale gas well for obtaining geological parameters in southern

Sichuan, and was cored with a total core length of 101.3 m in the Niutitang Formation and used in this study (Table 1).

2.2 Mercury intrusion and pore characteristics

Pore structure characterization of shale samples includes measuring their porosity, particle and bulk density, total pore surface area, and pore size distribution with mercury injection capillary pressure (MICP). Porosity and pore-throat distribution were analyzed using a mercury intrusion porosimeter (AutoPore IV 9510; Micromeritics Instrument

Corporation, Norcross, GA). In addition, the MICP approach can also indirectly evaluate other pore characteristics, such as permeability and tortuosity (Webb 2001; Gao and Hu 2013).

Each shale sample (rectangular prisms with the largest linear dimension at either 10 or 15 mm) was oven-dried at 60 °C for at least 48 h to remove moisture, and cooled to room temperature (~23 °C) in a desiccator with less than 10 % relative humidity before the MICP test. Samples were then evacuated to 50 μm Hg (6.7 Pa, or 99.993 % vacuum). During a MICP test, each sample underwent both low-pressure and high-pressure analyses. The highest pressure produced by our MICP instrument is 60,000 psia (413 MPa), corresponding (via the Washburn equation) to a pore-throat diameter of about 3 nm. Under low-pressure analysis, the largest pore-throat diameter recorded by MICP is about 36 μm for a narrow-bore sample holder (called penetrometer) for samples with low (down to about 0.5 %) porosity. Equilibration time (minimum elapsed time with mercury volume change <0.1 μL, before proceeding to the next pressure) was chosen to be 50 s.

As reported by Gao and Hu (2013), permeability for the shale samples was calculated from the MICP data by the method of Katz and Thompson (1986, 1987). Effective tortuosity τ , another important parameter which indicates pore connectivity, can also be derived from MICP data (Hager 1998; Webb 2001).

$$\tau = \sqrt{\frac{\rho}{24k(1 + \rho V_{tot})} \int_{\eta=r_{c,min}}^{\eta=r_{c,max}} \eta^2 f_V(\eta) d\eta}, \tag{1}$$

where ρ is fluid density, g/cm³; k is permeability, μm²; V_{tot} is total pore volume, mL/g; $\int_{\eta=r_{c,min}}^{\eta=r_{c,max}} \eta^2 f_V(\eta) d\eta$ is pore-throat volume distribution by pore-throat size. Effective tortuosity τ is related to the effective diffusion coefficient and travel distance of molecules by the following equation (Epstein 1989; Hu and Wang, 2003; Gommès et al. 2009):

$$\tau = \frac{D_0}{D_e} = \frac{1}{\phi} \left(\frac{L_e}{L} \right)^2, \tag{2}$$

where D_0 is the aqueous diffusion coefficient and D_e effective diffusion coefficient in porous media, m²/s; L_e is actual distance, m, traveled by a fluid particle as it moves between two points in a porous medium, which are separated by a straight line distance L , m; ϕ is porosity.

2.3 Spontaneous fluid imbibition and tracer migration

Because the concentration profile of various tracers provides a useful indication of the connectivity of a porous medium (Hu et al. 2012; Ewing et al. 2012), tracers were emplaced several different ways: by spontaneous

imbibition (Sect. 2.3), by diffusion (Sect. 2.4), and by injection under pressure (Sect. 2.5).

Spontaneous imbibition is a capillary force-driven process during which a wetting fluid displaces a non-wetting fluid only under the influence of capillary pressure. Because of the mathematical analogy between diffusion and imbibition, liquid imbibition can be used to probe a rock’s pore connectivity (Hu et al. 2012). Imbibition tests, which are much faster than diffusion tests, involve exposing one face of a rock sample to liquid (for example, water, API brine or n-decane), and monitoring the fluid mass uptake over time (e.g., Hu et al. 2001; Schembre and Kovscek 2006). Using the network modeling results of Ewing and Horton (2002), we can probe pore connectivity, as indicated by the slope of log (imbibed liquid mass) versus log (time). The imbibition behavior—whether the imbibition slope is 1/4, 1/4 changing to 1/2, or 1/2 —conveniently classifies a rock’s pore connectivity (Hu et al. 2012).

All sides of cm-sized cubes, except the top and bottom, were coated with quick-cure transparent epoxy to avoid evaporation of the imbibing fluid from, and reduce vapor transport and capillary condensation through, the side surfaces of the sample. The experimental procedure and data processing of imbibition tests were described in detail by Hu et al. (2001). Samples were first oven-dried at 60 °C for at least 48 h, in order to achieve a constant initial water saturation state, before being subjected to the imbibition experiments. During the imbibition tests with water or API brine, beakers of water were placed inside the experimental chamber to maintain a high and constant humidity level; these water beakers were removed for n-decane imbibition. The top of the side-epoxied samples was loosely covered with thin Teflon film, with a small hole left for air escape and co-current imbibition. The sample bottom was submerged to a depth of about 1 mm in the fluid reservoir. The imbibition rate was monitored by automatically recording the sample weight change over time.

In addition to replicate imbibition tests with de-ionized water being performed on the same sample (re-dried between runs), tracer imbibition experiment was conducted in API brine or n-decane fluid. Shales contain distinct phases of oil-wetting organic matter (e.g., kerogen) and water-wetting minerals, and tracers in two fluids (API brine and n-decane) are used to interrogate the wettability and connectivity of organic matter and mineral pore spaces. The organic fluid (n-decane) is expected to be preferentially attracted to the hydrophobic component (e.g., organic particles) of the shale matrix, with reported organic (kerogen) particle sizes ranging from less than 1 μm to tens of μm (Loucks et al. 2009; Curtis et al. 2012). Organic grains are found to be dispersed through the Barnett shale matrix (Hu and Ewing 2014), with their connection to

mineral phases unknown. An understanding of the distribution and migration of the hydrocarbons stored in pores in these organic grains is critically needed.

API brine is made of 8 % NaCl and 2 % CaCl₂ by weight (Crowe 1969). Tracer imbibition test of API brine contains both non-sorbing (perrhenate) and sorbing (cobalt, strontium, cesium, and europium, with different sorption extents) tracers, and were prepared using ultrapure (Type 1) water and >99 % pure reagents (NaReO₄, CoBr₂, SrBr₂·2H₂O, CsI, and EuBr₃·6H₂O; Sigma-Aldrich Co., St. Louis, MO). Concentrations used were 100 mg/L KReO₄, 400 mg/L CoBr₂, 400 mg/L SrBr₂, 100 mg/L CsI, and 200 mg/L EuBr₃.

Dissolved in *n*-decane, organic phase tracer chemicals were >99 % pure tracer element-containing organic reagents: 1-iododecane {CH₃(CH₂)₉I, molecular weight of 268.18 g/mol} and trichlorooxobis (triphenylphosphine) rhenium(V){[(C₆H₅)₃P]₂ReOCl₃, molecular weight 833.14 g/mol}. The elements iodine (I) and rhenium (Re) of these organic chemicals are detected by LA-ICP-MS for the presence of these two organic tracers in shale. Trichlorooxobis (triphenylphosphine) rhenium (referred as organic-Re in this paper) was first dissolved in acetone solvent until over-saturation, filtered to obtain the saturated liquid, and then added to *n*-decane at a volume ratio of 2 %. Organic-I (1-iododecane) was directly added to *n*-decane fluid at a volume ratio of 1 %.

We use jmol software (<http://jmol.sourceforge.net/>) to estimate the structural dimensions of these organic tracers. The organic-I has a diameter at 1.39 nm length (L) × 0.29 nm width (W) × 0.18 nm height (H), while the structural dimensions of organic-Re molecules are 1.27 nm L × 0.92 nm W × 0.78 nm H, with its width and height larger than organic-I.

After tracer imbibition tests of 12–24 h in either API brine or *n*-decane fluids, the shale samples were lifted out of the fluid reservoir, flash-frozen with liquid nitrogen, kept at –80 °C in a freezer, freeze-dried as a batch at –50 °C and near-vacuum (less than 1 Pa) for 48 h, then stored at <10 % relative humidity prior to the analyses by laser ablation inductively coupled plasma-mass spectrometry (LA-ICP-MS).

2.4 Saturated diffusion

Chemical diffusion within fluid-saturated shale was measured following Hu and Mao (2012). Dry shale samples were evacuated for nearly 24 h at 99.99 % vacuum, and saturated by allowing non-traced fluid to invade the evacuated sample. Samples were then exposed (1 face only) to a tracer-containing fluid (either API brine or *n*-decane) in a reservoir. At fixed diffusion times (generally 1 day for 1 cm-sided cubes, and 2–4 days for 1.5-cm cubes),

individual shale samples were removed from the reservoir and processed (liquid nitrogen freezing, freeze-drying, and dry-storing) for tracer mapping.

2.5 Wood's metal intrusion

Wood's metal intrusion, and consequent SEM imaging and LA-ICP-MS mapping, provides a direct assessment of surface-accessible pore structure. Rock pore networks are examined by injecting the sample with molten Wood's metal alloy (50 % Bi, 26.7 % Pb, 13.3 % Sn, and 10 % Cd; melting point around 78 °C), a method pioneered by Swanson (1979) and Dullien (1981). Because of its high bismuth (Bi) content, Wood's metal alloy does not shrink as it solidifies (Hildenbrand and Urai 2003). Because this metal alloy is solid below 78 °C, pore structures filled by Wood's metal alloy can be readily imaged and mapped for the presence of alloy component elements. Injecting molten Wood's metal alloy also offers the possibility of "freezing" the invaded network at any stage of the injection, allowing micro-structural studies to be made on the iteratively filled pore networks (Kaufmann 2010).

Wood's metal alloy impregnation on shales was carried out at Kaufmann's laboratory at Empa (Zurich, Switzerland), which is capable of injecting the alloy at pressures up to 6000 bars (600 MPa or 87,023 psi). This corresponds to a pore-throat diameter of 2.35 nm; this estimation is based on the Washburn equation (1921), using a surface tension of 0.4 N/m and a contact angle of 130° for Wood's metal (Darot and Reuschle 1999). Shale samples (about 5 × 5 × 5 mm³) were first dried at 110 °C for 1 week, then glued to the bottom of a cell, which was then filled with solid Wood's metal pieces. The cell was closed by a piston and heated to 85 °C under vacuum (<5 Pa); O-rings connecting the piston to the cell wall are able to bear pressures of more than 6,000 bars (Kaufmann 2010). Once the metal was molten, a load was applied to the piston by means of a press in controlled load mode. Pressure in the cell was increased by 7 MPa/min until the maximum pressure was reached; the maximum pressure was then held for 15 min. After that, the temperature was decreased at a cooling rate of about 1 °C/min to solidify Wood's metal in the intruded pore spaces. During this solidifying step, the load was regulated to maintain the desired pressure. Once cool, the alloy-impregnated sample was taken out of the cell and cut horizontally in the middle of the sample height, to allow tracing Wood's metal alloy intrusion from the sides. One piece was cut to 150 μm thick, polished, and mounted on a glass slide, and imaged with an environmental SEM (Quanta 200, FEI, Hillsboro, OR) using back-scattered electrons (Dultz et al. 2006). The other cut piece was used for LA-ICP-MS elemental mapping, using the distribution of Wood's metal alloy component (e.g., Pb) to identify surface-accessible connected pore spaces.

2.6 LA-ICP-MS elemental mapping

For tracer imbibition, saturated diffusion, and Wood's metal intrusion tests, tracer concentrations at spatially resolved (mostly at 100 μm for cm-sized samples) locations were measured using laser ablation followed by LA-ICP-MS. The laser ablation system (UP-213, New Wave; Fremont, CA) used a 213 nm laser to vaporize a hole in the shale sample at sub-micron depths; elements entrained in the vapor were analyzed with ICP-MS (PerkinElmer/SCIEX ELAN DRC II; Sheldon, CT). For various tests described here, this LA-ICP-MS approach can generate 2-D and 3-D maps of chemical distributions in rock at a spatial resolution of microns, and a concentration limit of low mg/kg (Hu et al. 2004; Hu and Mao 2012; Peng et al. 2012).

First we spot-checked for the presence of tracers at the sample's bottom (reservoir) and top faces, then the sample was cut dry in the middle from the top face, transverse-wise with respect to the imbibition/diffusion direction. A grid of spot analyses were then performed by LA-ICP-MS on the saw-opened interior face to map the tracer distribution within the shale sample, with a two-grid scheme to capture the tracer penetration into the samples from the edge. The first grid used an area of about 10 mm \times 0.3 mm (in the direction of imbibition/diffusion), close to the sample bottom, with 100 μm laser spot size and 100 μm spacing between spots in the imbibition/diffusion direction. This fine gridding scheme was performed in the area close to the bottom of the sample in the flow direction, because this area can have a steep tracer concentration gradient over a short distance. A second grid was then used to the right of the first grid at \sim 800 μm spacing among laser spots to capture the possible presence of tracers away from the bottom edge.

3 Results and discussion

3.1 Mercury intrusion

As measured by MICP, pores in American and Chinese shales are predominantly in the nm size range with a measured median pore-throat diameter of 4.1–65.9 nm (Table 2). Excluding a few samples with fractures, 80 %–95 % of matrix pore-throat sizes by volume are smaller than 100 nm. For example, duplicate measurements of Longmaxi Formation samples (LMX TZ-4H in Table 2) show a porosity of 3.83 % and 5.45 %, median pore-throat sizes of 6.3 and 5.0 nm, with nearly 50 % of the pore-throat sizes located in 3–5 nm range and 90 %–95 % smaller than 100 nm. This is consistent with other literature values. For the Longmaxi shale samples from the

Changxin#1 well drilled in southeastern region of the Sichuan Basin, Chen et al. (2013) reported that the average porosity is 5.68 %. The micropores in the shale observed by the SEM are dominated by intergranular (dissolution) mineral pores, intergranular gaps, intragranular pores, the organic matter micropores, and micro-fractures. The mercury intrusion porosimetry results show that the maximum radius of the pore-throat is 33 nm, with the average at 10 nm (Chen et al. 2013).

While the presence of nanopores in shales has been well recognized since the first application of Ar-ion milling and field-emission SEM imaging (Loucks et al. 2009) to indicate the dominant organic nanopores in Barnett shales, larger pores cannot be discounted in their roles of mass transport and connecting nanopore regions. Pores less than 3 nm can be quantified with approaches such as low-pressure gas sorption isotherm, but such small pores probably do not play critical roles in hydrocarbon movement (Javadpour et al. 2007). When small pores or narrow pore-throats have diameters in the same order of magnitude as the chemicals, the steric hindrance effect can be significant (Hu and Wang 2003). Most hydrocarbon species of interests have a molecular diameter from 0.5 to 10 nm (Nelson 2009), and therefore probably the pore systems that contribute to hydrocarbon movement are these connected ones with pore sizes of 5–100 nm.

Using SEM/field-emission SEM methods to determine porosities of a range of shale, Slatt and O'Brian (2011) and Slatt et al. (2013) reported that micropores ($>1 \mu\text{m}$ in pore length and nanopores ($<1 \mu\text{m}$) are subequal. The micropores are commonly porous floccules (clumps of electrostatically charged clay flakes arranged in edge-face or edge-edge card house structure) of up to 10 μm in diameter, which are not often seen or identified in ion-milled shale surfaces, perhaps due to the collapse of floccules during milling (Slatt et al. 2013). For the Eagle Ford shale with a high carbonate content, Slatt et al. (2012) reported the presence of μm -sized pore types from coccospheres (internal chambers and hollow spines are up to 1 μm in diameter and several μm in length) and foraminifera (their internal chambers can be 10 μm in diameter). Our MICP analyses, performed on individual 1 cm sized cubes, observed appreciable μm -sized pores, with $>1 \mu\text{m}$ sized pores account for 10 %–20 % for American and Chinese shales studied in this work.

Since core samples are not readily available, we compare the outcrop with core samples for Eagle Ford Lower Shale, and observe a quite different behavior. The outcrop sample has a unimodal pore-throat size (at 95 %) located at 10–50 nm, compared to 30 %–44 % for three core samples. Pore-throats for the core samples are widely distributed from 3 nm to 36 μm , though most of them (70 %–80 %) are smaller than 100 nm. The disparity between

Table 3 Experimental imbibition results for Eagle Ford Leppard #1 well samples

Sample ID	Sample dimension	Height/width	Imbibition slope ^a
EF LP-4144	1.10 cm L × 1.00 cm W × 1.56 cm H	1.49	0.266 ± 0.073 (N = 5)
EF LP-4146	1.03 cm L × 1.38 cm W × 1.35 cm H	1.12	0.350 ± 0.059 (N = 3)
EF LP-4155	1.50 cm L × 0.97 cm W × 4.06 cm H	3.29	0.312 ± 0.042 (N = 4)
EF LP-4157	1.12 cm L × 1.14 cm W × 2.43 cm H	2.14	0.295 ± 0.018 (N = 4)
EF LP-4166	1.19 cm L × 1.44 cm W × 1.83 cm H	1.39	0.256 ± 0.008 (N = 3)

^a Average ± standard deviation for replicate measurements on the same sample

outcrop and core samples is also reflected in median pore-throat sizes, as well as permeability with a difference of a factor of 100. However, caution needs to be extended when using data from outcrop samples to infer underground conditions.

Matrix permeabilities for these twelve American and Chinese shales, at a total of 24 MICP measurements, are 0.52–9.6 nD (Table 2), as estimated by the method of Katz and Thompson (1986, 1987). This is consistent with reported permeabilities of 1–10 nD by Heller and Zoback (2013), who used a pulse-decay permeameter with helium (more labor- and instrumentation-intensive) on 1–2 mm sized Barnett chips. The matrix permeabilities for Lower Eagle Ford shale from a well at different depths (4053.2 to 4087.8 m) range from 0.44 to 23.3 nD (5.82 ± 6.89 , $N = 14$) (David Maldonado, 2012, personal communication), measured by the Gas Research Institute (GRI) (crushed rock) method (Luffel et al. 1993; Guidry et al. 1996). Our MICP technique, with cm-sized samples under confined pressure conditions and at an analytical cost (and sample mass) required of less than 10 % of amount of sample required for the GRI method, consistently produces comparable permeability values of 1.60–2.97 nD for the Leppard #1 core samples (Table 2).

MICP data can also be used with Hager's (1998) method to estimate effective tortuosity values, which characterize the convoluted pathways of fluid flow through porous systems (e.g., Epstein 1989; Hu and Wang 2003; Gommes et al. 2009). Following Gommes et al. (2009) approach (Eq. 2) of relating geometrical tortuosity to the travel paths that molecules will need to follow through a porous medium, the L_c/L ratios for the American and Chinese shales are on the order of 2–11 (Table 2). These relatively large values of tortuosity imply that fluid within the tight shale formations will need to make its way through some tortuous pathways in order to migrate from one location to another. For example, a tortuosity L_c/L of 11 for Longmaxi Formation sample means that it will take 11 cm for fluid to travel a linear distance of 1 cm in that formation. This is consistent with the findings from other approaches presented in this paper, which indicate that the nanopores of the tight shale formations are poorly connected so that

fluids require much time to find connected pathways to travel a limited distance.

3.2 Spontaneous fluid imbibition and tracer migration

Imbibition experiments for American shales consistently produce imbibition slopes of approximately $\frac{1}{4}$. The results for Eagle Ford core samples are presented in Table 3, with a typical one shown in Fig. 1; similar results are presented for Barnett core samples in Hu and Ewing (2014). The $\frac{1}{4}$ imbibition slope was consistently observed across different sample shapes, and imbibition directions (parallel/horizontal versus transverse/vertical to the bedding plane) examined for Barnett samples, and for all sample depths (e.g., Table 3). From this, we conclude that pores in the Eagle Ford and Barnett shales are poorly connected for water movement, with a correlation length (imbibition distance beyond which behavior becomes Fickian) greater than the sample height (approximately 15 mm) used. On other rocks, we have experimentally observed all three types of imbibition slopes ($\frac{1}{4}$, $\frac{1}{4}$ changing to $\frac{1}{2}$, and $\frac{1}{2}$), consistent with percolation theory (Stauffer and Aharony 1994; Hunt et al. 2014). For example, Hu et al. (2012)

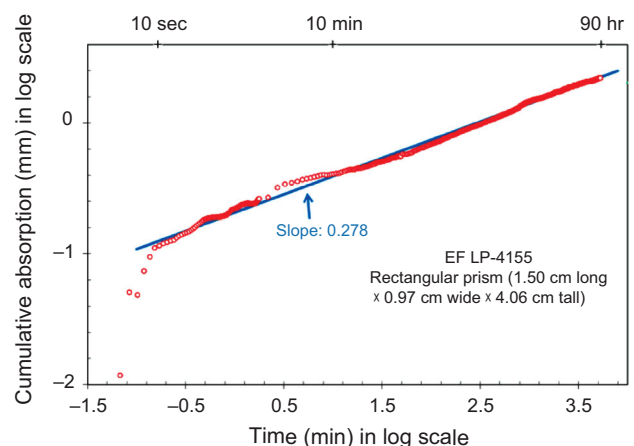


Fig. 1 Water imbibition results for Leppard #1 well 4155 m core sample of Eagle Ford shale

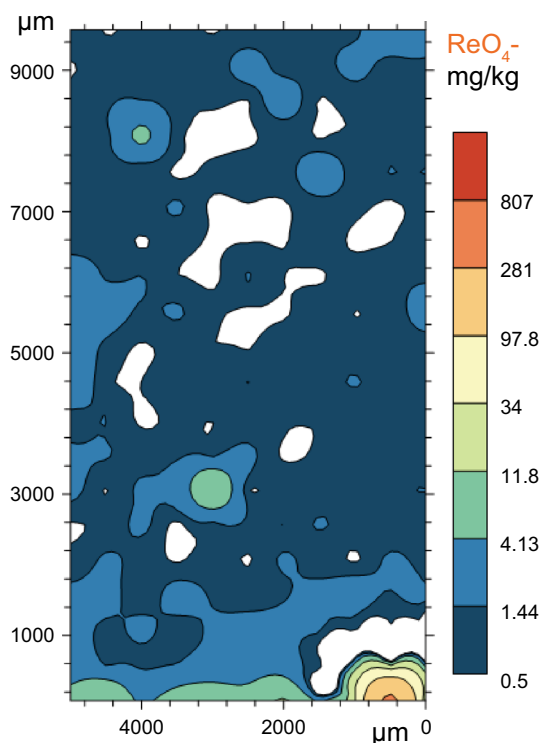


Fig. 2 API brine-tracer imbibition penetration profile in LMX TZ-4H sample of Longmaxi shale, mapped on the interior face for non-sorbing ReO_4^- ; imbibition time 47.5 h. This $5000 \mu\text{m} \times 9575 \mu\text{m}$ grid nearly covers whole sample, with a mapping routine of $100 \mu\text{m}$ laser spot size and $500 \mu\text{m}$ spacing between spots. The *bottom* (tracer imbibing) *face* is shown to the *bottom* of the figure. The LA-ICP-MS detection limit and background levels in the clean sample for Re are about 0.05 and 0.5 mg/kg (used as the smallest value for 8-scale color scheme), respectively. The largest value of color scale (807 mg/kg) is the averaged Re concentration of 81 measurements obtained on the imbibing face (807 ± 391 mg/kg)

observed the $\frac{1}{2}$ slope across all aspect ratios for Berea sandstone samples, indicating its well-connected pore spaces.

In addition to fluid imbibition tests to probe the pore connectivity, some tracer imbibition tests were conducted and resultant tracer penetration distance was mapped using LA-ICP-MS. The mapping result for API brine-tracer imbibition into the interior face of a Longmaxi shale sample (LMX DZ-4H) is shown in Fig. 2. When imbibition proceeds from this initially dry sample, capillary-driven advective flow produces a relatively steep imbibition front for non-sorbing ReO_4^- . At about 1 mm into the matrix from the edge, the tracer is only distributed at about 1–4 mg/kg (compared with a measured mean concentration of 807 mg/kg within $2 \mu\text{m}$ of the edge on the imbibing face; in other words, the connected porosity away from the edge is only about 0.5 %–2 % of the total pore space), from the imbibition test of 47.5 h. Such a result indicates the limited pore connectivity for brine fluid flow and tracer

movement, with the connected pore spaces limited to the sub-mm range from the sample edge in Longmaxi shale; similar results are observed for Barnett shale (Hu and Ewing 2014).

3.3 Saturated diffusion

Figure 3 presents 2-D tracer concentration profiles in n-decane fluid for a Niutitang shale (NTT JY#1-137) after 25 h diffusion time. Two molecular tracers in n-decane fluid have the sizes of $1.39 \text{ nm} \times 0.29 \text{ nm} \times 0.18 \text{ nm}$ for organic-I (Fig. 3a) and $1.27 \text{ nm} \times 0.92 \text{ nm} \times 0.78 \text{ nm}$ for organic-Re (Fig. 3b). Much less diffusive penetration was observed for larger molecules of organic-Re inside a sample with 47 %–66 % pore-throat sizes between 3–50 nm (measured characteristic pore-throat sizes from MICP are 6.5–11.0 nm, when fluid mercury starts to percolate across the whole sample; Table 2). This result indicates the entanglement of nano-sized molecules in nanopore spaces of tight samples. Comparatively, the narrower sized organic-I is present nearly throughout the whole sample, indicating that this shale sample has oil-wetting characteristics and possesses well-connected pore spaces for hydrophobic molecules to move, barring the very sensitive molecular size effect. The practical implication is that the out-diffusion of nm-sized hydrocarbon is expected to be slow, of limited quantity, and largely limited to a small distance from rock matrix into a fracture; this will affect the hydrocarbon recovery in stimulated shale reservoirs.

3.4 Limited edge-accessible porosity from Wood's metal intrusion

The Barnett shale sample from 2185 m (B BL-2185) was injected with Wood's metal alloy at 1542 bars (154 MP). At this pressure, pore-throats of diameter greater than 9.2 nm are invaded. For this sample, SEM images show that there is little connected matrix porosity farther than about $60 \mu\text{m}$ from the sample's edge (figure not shown); Wood's metal mainly occupies small cracks and matrix pores connected to the sample surface. As in the case for mercury intrusion, the sample was externally and uniformly surrounded by non-wetting molten Wood's metal alloy, with even pressurization to reduce experiment-related fractures.

The sample was also mapped by LA-ICP-MS for more sensitive detection of the presence of Wood's metal component elements (Bi, Cd, Pb, and Sn). Distribution of all these elements inside the shale sample was similar, so only the plot for Pb is presented (Fig. 4). Wood's metal alloy has 26.7 % Pb (267,000 mg/kg), consistent with the

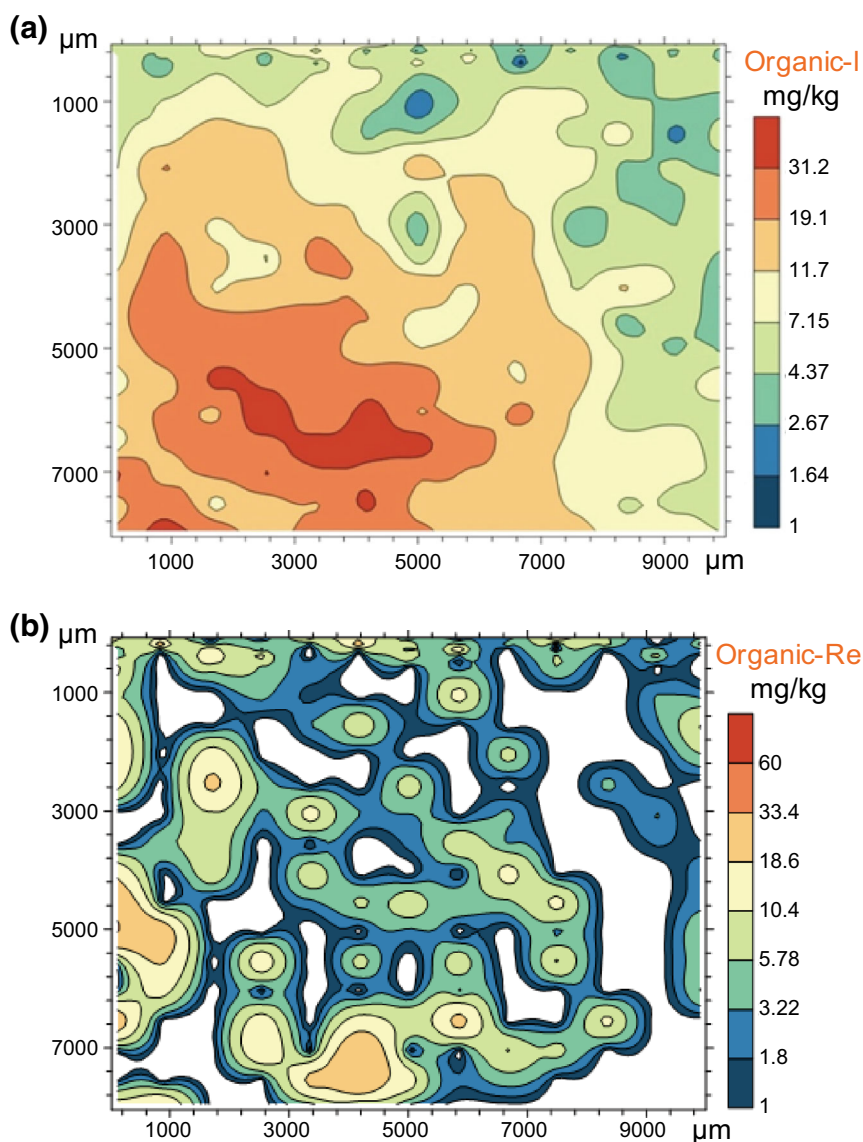


Fig. 3 Saturated diffusion test results for NTT JY#1-137 sample of Niutitang Shale Formation using n-decane fluid with tracers of organic iodine and organic rhenium of different molecular sizes. The total grid size is 10,000 μm \times 8050 μm to cover whole sample, and mapped with a 100 μm laser spot size and two-grid scheme of variable spacing between spots; the white areas indicate the regions of concentration below the LA-ICP-MS detection limit

concentration detected by LA-ICP-MS, but its natural abundance in the shale matrix is only about 0.5 mg/kg. Lead is, therefore, an excellent proxy for the presence of Wood's metal inside the sample, identifying porous regions that are connected to the sample's exterior. LA-ICP-MS has a higher chemical resolution and larger observation scales than SEM, though lower spatial resolution, and reveals connected pore spaces that are not visible with SEM imaging. Wood's metal penetrates all pore spaces (at the resolution of 100- μm laser spot) within this sample with a dimension of 7.0 mm \times 7.75 mm, as seen from the

concentrations uniformly across the sample at above the 0.5 mg/kg background level. However, the surface-accessible connected pores constitute a very low percentage of the interior volume. Detected Pb concentrations in the interior area are only in the range of 10,000 mg/kg, compared to 267,000 mg/kg for the Pb content in Wood's metal itself. Even under a high pressure of 1542 bars, a mean connected porosity therefore comprises about 4 % of interior pore volume of this sample, consistent with other results of this work with respect to limited pore connectivity for tight shales.

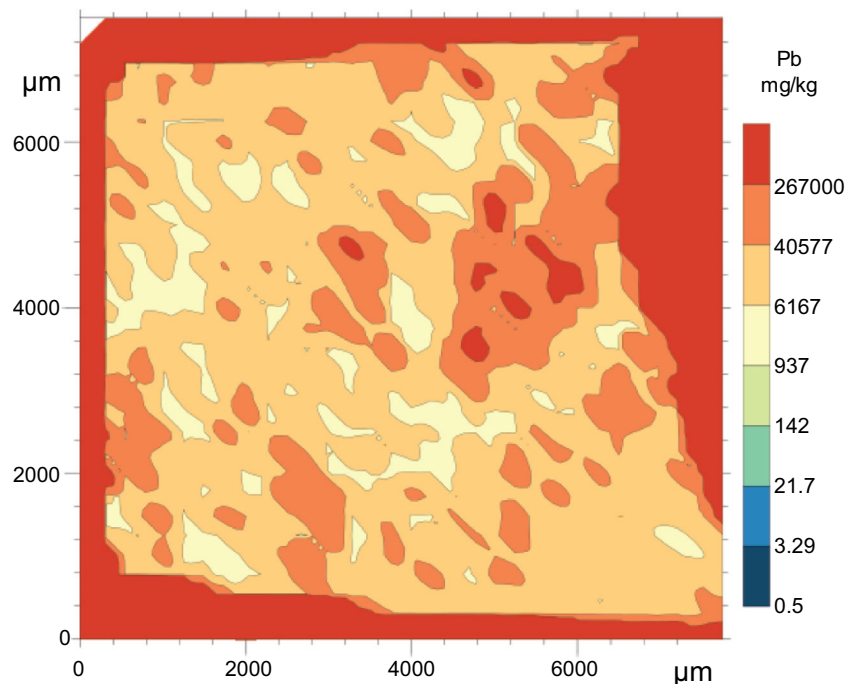


Fig. 4 2-D LA-ICP-MS mapping of Pb (lead) distribution in B BL-2185 m sample following Wood’s metal alloy injection at a pressure of 1542 bars; laser spot size is 100 μm and spacing between spots is 250 μm

4 Conclusions

We investigated pore geometry and topology in several typical American and Chinese shales, and their implications for fluid movement and tracer migration. Our experimental approaches included mercury porosimetry, spontaneous imbibition and tracer migration, tracer diffusion, and Wood’s metal intrusion under high pressures. Consistent with other reports, we found that these shale pores are predominantly in the nm size range, with a median pore-throat diameter of 4.1–65.9 nm. It is expected that the shale’s geometrical properties—low porosity and small pore-throat size—will yield extremely low diffusion and imbibition rates.

Using multiple characterization approaches to infer the shale’s topology, we also found consistent evidences that pore connectivity in these shales could be quite low for a particular probing fluid of either API brine or n-decane. Tracer diffusion inside the shale matrix was not well described by classical Fickian behavior; the anomalous behavior suggested by percolation theory gave a better description. The spontaneous imbibition tests saw an imbibition slope characteristic of low-connectivity material. Our different methods assessing edge-accessible porosity—following spontaneous imbibition, diffusion, and high pressure intrusion—consistently showed a steep decline in accessible porosity with distance from the

sample exterior. In fact, Wood’s metal concentration in the interior is only about 4 % under high pressures, which indicates that only a limited number of the interior pores are connected to the outside by a continuous pathway.

Because shale has both mineral (water-wetting) and organic (kerogen; water-repelling) pores, a fluid-based approach such as spontaneous imbibition and diffusion are expected to give lower accessible porosity profiles than will pressure-injected Wood’s metal, which accesses both the water-wet and oil-wet pores. But despite Wood’s metal accessing both kinds of pores, it consistently shows the steep decline in accessible porosity with distance that is characteristic of low pore connectivity. All results converge into findings that pores more than a few mm inside a sample are unlikely to be connected to the exterior, with additional implications of molecular size effects, as shown from our tracers of different sizes. In terms of hydrocarbon production, matrix pores more than a few mm from an induced fracture are only sparsely connected to fracture network and the producing borehole.

The consequences of low pore connectivity, specifically distance-dependent accessible porosity, will lead to an initial steep decline in production rates and low overall recovery. Once the hydrocarbons residing in the fracture network are exhausted, hydrocarbon replenishment from shale matrix (i.e., “matrix feeding”) is limited by the slower anomalous diffusion through the shale matrix, and

reduced by the fraction of the matrix that is actually accessible.

This study addresses knowledge gaps regarding pore connectivity in typical American and Chinese shales. We show that pore connectivity may be a dominant constraint on diffusion-limited hydrocarbon transport. Pore connectivity at the nanoscale may be the cause of underlying steep first-year declines in hydrocarbon production, as well as the low overall recovery observed in hydraulic fractured shales.

Acknowledgments Funding for this project was partially provided by the following three State Key Laboratories in China: State Key Laboratory of Oil and Gas Reservoir Geology and Exploitation, Chengdu University of Technology, Chengdu (PLC-201301); State Key Laboratory of Organic Geochemistry, Chinese Academy of Sciences, Guangzhou (No. OGL-201402); the Foundation of State Key Laboratory of Petroleum Resources and Prospecting, China University of Petroleum, Beijing (No. PRP/open-1403). The authors would like to thank Harold Rowe and Roger Slatt for providing Barnett and Eagle Ford samples. Laboratory assistance from Troy Barber, Yuxiang Zhang, Golam Kibria, and Francis Okwuosa is also much appreciated.

Open Access This article is distributed under the terms of the Creative Commons Attribution 4.0 International License (<http://creativecommons.org/licenses/by/4.0/>), which permits unrestricted use, distribution, and reproduction in any medium, provided you give appropriate credit to the original author(s) and the source, provide a link to the Creative Commons license, and indicate if changes were made.

References

- Bear J. Dynamics of fluid in porous media. New York: Dover Publications; 1972.
- Chen WL, Zhou W, Luo P, et al. Analysis of the shale gas reservoir in the Lower Silurian Longmaxi Formation, Changxin 1 well, Southeast Sichuan Basin, China. *Acta Petrol Sin.* 2013;29(3):1073–86 (in Chinese).
- Crowe CW. Methods of lessening the inhibitory effects to fluid flow due to the presence of solid organic substances in a subterranean formation. U.S. Patent Office 3482636, patented on 9 Dec 1969.
- Curtis JB. Fractured shale-gas systems. *AAPG Bull.* 2002;86(11):1921–38.
- Curtis ME, Cardott BJ, Sondergeld CH, et al. Development of organic porosity in the Woodford shale with increasing thermal maturity. *Int J Coal Geol.* 2012;103:26–31.
- Darot M, Reuschle T. Direct assessment of Wood's metal wettability on quartz. *Pure Appl Geophys.* 1999;155(1):119–29.
- DOE (Department of Energy). Modern shale gas development in the United States: A primer. 2009.
- Dullien FAL. Wood's metal porosimetry and its relation to mercury porosimetry. *Powder Tech.* 1981;29:109–16.
- Dullien FAL. Porous media: fluid transport and pore structure. 2nd ed. San Diego: Academic Press; 1992.
- Dultz S, Behrens H, Simonyan A, et al. Determination of porosity and pore connectivity in feldspars from soils of granite and saprolite. *Soil Sci.* 2006;171(9):675–94.
- EIA (Energy Information Administration). Annual energy outlook 2014: with projections to 2040. U.S. Department of Energy, DOE/EIA-0383, released on May 7, 2014. Available at <http://www.eia.gov/forecasts/AEO/>. Accessed 28 Jan 2015.
- Epstein N. On tortuosity and the tortuosity factor in flow and diffusion through porous media. *Chem Eng Sci.* 1989;44(3):777–9.
- Ewing RP, Horton R. Diffusion in sparsely connected pore spaces: temporal and spatial scaling. *Water Resour Res.* 2002;38(12):1285. doi:10.1029/2002WR001412.
- Ewing RP, Liu CX, Hu QH. Modeling intragranular diffusion in low-connectivity granular media. *Water Resour Res.* 2012;48:W03518. doi:10.1029/2011WR011407.
- Gao ZY, Hu QH. Estimating permeability using median pore-throat radius obtained from mercury intrusion porosimetry. *J Geophys Eng.* 2013;10:025014. doi:10.1088/1742-2132/10/2/025014.
- Gommes CJ, Bons AJ, Blacher S, et al. Practical methods for measuring the tortuosity of porous materials from binary or gray-tone tomographic reconstructions. *AIChE J.* 2009;55:2000–12.
- Grieser WV, Shelley RF, Johnson BJ, et al. Data analysis of Barnett shale completions. *SPE J.* 2008. doi:10.2118/100674-PA.
- Guidry FK, Luffel DL, Curtis JB. Development of laboratory and petrophysical techniques for evaluating shale reservoirs. GRI (Gas Research Institute) Final Report GRI-95/0496, 1996.
- Guo TL. Evaluation of highly thermally mature shale-gas reservoirs in complex structural parts of the Sichuan Basin. *J Earth Sci.* 2013;24(4):863–73.
- Hager J. Steam drying of porous media. Ph.D. Thesis. Department of Chemical Engineering, Lund University, Sweden. 1998.
- Heller R, Zoback M. Laboratory measurements of matrix permeability and slippage enhanced permeability in gas shales. *Soc Pet Eng, SPE* 168856. 2013.
- Hildenbrand A, Urai JL. Investigation of the morphology of pore space in mudstones—first results. *Mar Pet Geol.* 2003;20(10):1185–200.
- Hoffman T. Comparison of various gases for enhanced oil recovery from shale oil reservoirs. This paper was presented for presentation at the eighteenth SPE improved oil recovery symposium held in Tulsa, OK, pp. 14–18, SPE 154329. 2012.
- Hu QH, Wang JSY. Aqueous-phase diffusion in unsaturated geological media: a review. *Crit Rev Environ Sci Technol.* 2003;33(3):275–97.
- Hu QH, Mao XL. Applications of laser ablation-inductively coupled plasma-mass spectrometry in studying chemical diffusion, sorption, and transport in natural rock. *Geochem J.* 2012;46(5):459–75.
- Hu QH, Ewing RP. Comment on “Energy: a reality check on the shale revolution” (Hughes, J.D., *Nature*, Vol. 494, p. 307–308. doi:10.1038/494307a. <http://www.nature.com/nature/journal/v494/n7437/full/494307a.html>. Accessed 21 Feb 2013.
- Hu QH, Ewing RP. Integrated experimental and modeling approaches to studying the fracture-matrix interaction in gas recovery from Barnett Shale. Final Report, Research Partnership to Secure Energy for America (RPSEA), National Energy Technology Laboratory, Department of Energy. 2014.
- Hu QH, Persoff P, Wang JSY. Laboratory measurement of water imbibition into low-permeability welded tuff. *J Hydrol.* 2001;242(1–2):64–78.
- Hu QH, Ewing RP, Dultz S. Pore connectivity in natural rock. *J Contam Hydrol.* 2012;133:76–83.
- Hu QH, Kneafsey TJ, Wang JSY, et al. Characterizing unsaturated diffusion in porous tuff gravels. *Vadose Zone J.* 2004;3(4):1425–38.
- Hughes JD. Drill, Baby, Drill: can unconventional fuels usher in a new era of energy abundance? Post Carbon Institute. 2013a.
- Hughes JD. Energy: a reality check on the shale revolution. *Nature.* 2013;494:307–8.
- Hunt AG, Ewing RP, Ghanbarian B. Percolation theory for flow in porous media. 3rd ed., Lecture notes in physics Heidelberg: Springer; 2014. p. 880.

- Jarvie DM. Shale resource systems for oil and gas: part 1—shale-gas resource systems. In: Breyer JA, editor, *Shale reservoirs—giant resources for the 21st century*. AAPG Memoir; 2012, 97: 69–87.
- Javadpour F, Fisher D, Unsworth M. Nanoscale gas flow in shale gas sediments. *J Can Pet Technol*. 2007;46(10):55–61.
- Katz AJ, Thompson AH. A quantitative prediction of permeability in porous rock. *Phys Rev B*. 1986;34:8179–81.
- Katz AJ, Thompson AH. Prediction of rock electrical conductivity from mercury injection measurements. *J Geophys Res*. 1987;92(B1):599–607.
- Kaufmann J. Pore space analysis of cement-based materials by combined nitrogen sorption: Wood's metal impregnation and multi-cycle mercury intrusion. *Cement Concr Compos*. 2010;32(7):514–22.
- King GE. Hydraulic fracturing 101. *SPE* 152596. 2012.
- Liu SG, Ma WX, Luba J, et al. Characteristics of the shale gas reservoir rocks in the Lower Silurian Longmaxi Formation, east Sichuan Basin, China. *Acta Petrol Sin*. 2011;27(8):2239–52 (in Chinese).
- Loucks RG, Reed RM, Ruppel SC, Jarvie DM. Morphology, genesis, and distribution of nanometer-scale pores in siliceous mudstones of the Mississippian Barnett Shale. *J Sediment Res*. 2009;79(11–12):848–61.
- Loucks RG, Ruppel SC. Mississippian Barnett Shale: lithofacies and depositional setting of a deep-water shale-gas succession in the Fort Worth Basin, Texas. *AAPG Bull*. 2007;91(4):579–601.
- Luffel DL, Hopkins CW, Schettler PD. Matrix permeability measurement of gas productive shales. *SPE* 26633. 1993.
- Nelson PH. Pore-throat sizes in sandstone, tight sandstone, and shale. *AAPG Bull*. 2009;93(3):329–40.
- Nicot J-P, Scanlon BR, Reedy RC, Costley RA. Source and fate of hydraulic fracturing water in the Barnett shale: a historical perspective. *Environ Sci Technol*. 2014;48(4):2464–71.
- Peng S, Hu QH, Ewing RP, et al. Quantitative 3-D elemental mapping by LA-ICP-MS of basalt from the Hanford 300 area. *Environ Sci Tech*. 2012;46:2035–42.
- Schembre JM, Kovscek AR. Estimation of dynamic relative permeability and capillary pressure from countercurrent imbibition experiments. *Transp Porous Media*. 2006;65:31–51.
- Slatt RM, O'Brien NR. Pore types in the Barnett and Woodford gas shales: contribution to understanding gas storage and migration pathways in fine-grained rocks. *AAPG Bull*. 2011;95(12):2017–30.
- Slatt RM, O'Brien NR, Miceli R, et al. Eagle Ford condensed section and its oil and gas storage and flow potential. *AAPG Annual Convention and Exhibition, Long Beach, California, 22–25 April 2012*. Search and Discovery Article #80245. 2012.
- Slatt RM, O'Brien NR, Molinares-Blanco C et al. Pores, spores, pollen and pellets: small, but significant constituents of resources shales. *SPE* 168697/URTeC 1573336. 2013.
- Stauffer D, Aharony A. *Introduction to percolation theory*. 2nd ed. London: Taylor and Francis; 1994.
- Sun W, Liu SG, Ran B, et al. General situation and prospect evaluation of the shale gas in the Niutitang Formation of Sichuan Basin and its surrounding area. *J Chengdu Univ Technol (Science and Technology Edition)*. 2011;39(2):170–75 (in Chinese).
- Swanson BF. Visualizing pores and nonwetting phase in porous rock. *J Petrol Technol*. 1979;31:10–8.
- Washburn EW. Note on a method of determining the distribution of pore sizes in a porous materials. *Proc Natl Acad Sci USA*. 1921;7:115–6.
- Webb PA. *An introduction to the physical characterization of materials by mercury intrusion porosimetry with emphasis on reduction and presentation of experimental data*. Micromeritics Instrument Corporation. 2001.
- Xie GW, Zhou CM, McFadden KA, et al. Microfossils discovered from the Sinian Doushantuo Formation in the Jiulongwan section, East Yangtze Gorges area, Hubei Province, South China. *Acta Palaeontologica Sinica*. 2008;47(3):279–91 (in Chinese).
- Zou CN, Tao SZ, Yang Z, et al. Development of petroleum geology in China: discussion on continuous petroleum accumulation. *J Earth Sci*. 2013;24(4):796–803.